Electronic Supplementary Material (ESI) for Journal of Materials Chemistry A.

Supplementary Information

Shape-memory $V_3O_7 \cdot H_2O$ Electrocatalyst for Foldable N_2 Fixation

Yuntong Sun, Shan Ding, Chen Zhang, Jingjing Duan,* Sheng Chen*

Key Laboratory for Soft Chemistry and Functional Materials (Ministry of Education), School of Chemical Engineering, School of Energy and Power Engineering, Nanjing University of Science and Technology, Nanjing, 210094, China

E-mail: jingjing.duan@njust.edu.cn (J.D.); sheng.chen@njust.edu.cn (S.C.)

I. Experimental Section

1. Material Synthesis

Synthesis of $V_3O_7{\cdot}H_2O$ monolith. Firstly, 50 mg of VO $(acac)_2$ was dissolved in 30 mL of DI-water, followed by hydrothermally heated at 150 °C for 10 hours (hrs). After cooling down to room temperature, the mixture was taken out and washed with copious water. Next, different amount of the product was mixed with 5 mL of DI-water to form a homogeneous dispersion, which was freeze-dried by using liquid nitrogen.

Synthesis of $V_3O_7{\cdot}H_2O$ powder. The material was prepared through a similar procedure to 3D $V_3O_7{\cdot}H_2O$ monolith except of replacing freeze-dry by 60 °C dry in air.

2. Physical Characterization

Morphology was observed on field emission scanning electron microscope (FESEM, JEOL 7800F Prime), transmission electron microscope (TEM, FEI Titan 80-300, 300 kV acceleration voltage), and atomic force microscope (AFM, Bruker D8 SPM); energy-dispersive X-ray spectroscopy and element mapping were recorded on SEM (OXFORD X-MaxN 150 10 kV). Surface areas were tested on a Micromeritics ASAP 2020 Plus analyzer by Brunauer-Emmet-Teller (BET) adsorption-desorption isotherms at 77 K with corresponding pore size distributions estimated using Barrett-Joyner-Halenda (BJH) model. The crystalline structure was examined by X-ray diffractometer (XRD, Smartlab 9kw, 40 kV, 40 mA, λ=1.5418Å) with Cu -Kα radiation. Further, structure characterizations were performed on X-ray photoelectron

spectroscopy (XPS) collected between 0 and 1400 eV on an Axis Ultra (Thermo ESCALAB 250XI) XPS spectrometer equipped with an Al Kα source (1486.6 eV); Raman data were collected on an Aramis (HORIBA JOBIN YVON, Te RAMAN-1024x256-OPEN-SYN) spectroscopy using the excitation wavelength of 532 nm. Zeta potential was monitored on a Malvern ZS90 Zetasizer Nano series analyser; FTIR spectra were recorded on a Thermofisher NICOLETIS10 FTIR spectrometer. ^{1}H NMR spectra were collected on a superconducting-magnet NMR spectrometer (Bruker AVANCE III HD 500 MHz) and dimethyl sulphoxide was used as an internal to calibrate the chemical shifts in the spectra.

3. Electrochemical characterizations.

Working electrode and electrochemical setup for H-type cell. 5 mg of $V_3O_7{\cdot}H_2O$, 1 mg of acetylene black, 30 μL of Nafion solution (5 wt%) were dispersed in 1 mL of isoproponal/DI-water (4:1 v/v) by ultrasonication for 30 min to form a uniform catalyst ink. Next, 40 μL of the catalyst ink was transferred to a 1×0.7 cm^2 carbon fiber paper with a loading of 0.2 mg cm^{-2}, which was dried under ambient condition overnight.

All tests were performed on a CHI 760E electrochemical workstation. Under Ar- or N_2-saturated conditions, the synthesized catalyst, graphite rods, and $Hg/Hg_2Cl_2(S)/KCl$ (saturated) were used as the working, counter, and reference electrode. Nafion 211 was used as separator, while 0.1 M Na_2SO_4 and 0.05 M H_2SO_4 are used as electrolytes and exhaust gas absorption liquids.

Working electrode and electrochemical setup for flow-type cell. To make working

electrode, the above-mentioned uniform catalyst ink was transferred to a 3×1 cm^2 gas diffusion layer (GDL, effective catalytic area is 2×0.5 cm^2) with a loading of 0.2 mg cm^{-2}, which was dried under ambient condition overnight. Next, blank GDL substrate was used as counter electrode, Ag/AgCl (saturated) as reference electrode, and Nafion 211 as separator. In addition, 0.1 M Na_2SO_4 and 0.05 M H_2SO_4 are used as electrolytes and exhaust gas absorption liquids. The rate of electrolyte flow was 40 ml min^{-1}. Gas flow was 20 ml min^{-1}.

Electrochemical NRR testing. Prior to electrochemical testing, the electrolyte was purged with Ar or N_2 for 30 min. Next, 20-cycle voltametric scan (CV) was performed at a rate of 20 mV s^{-1} to activate the catalyst electrode. For NRR characterizations, a linear sweep voltammogram (LSV) was performed at a scan rate of 5 mV s^{-1} in the range of -0.8-0 V (*vs.* RHE). The potentiostatic test was carried out at different potentials for 2 hrs (in H-type cell) or 1 hr (in flow-type cell) under continuous saturation of Ar or N_2 flows. The data of first cycle was discarded to avoid possible ammonia pollution.

The NRR potential is referenced against reversible hydrogen electrode (RHE):

$$E_{RHE}=E_{Hg/Hg2Cl2}+0.059\times pH+0.242 \quad (1)$$

The Faradaic efficiency was calculated as follows:

$$FE=3F\times c(NH_3)\times V/(17\times Q) \quad (2)$$

And the ammonia yield rate was calculated as follows:

$$V(NH_3)=c(NH_3)\times V/(t\times m) \quad (3)$$

where F is the Faradaic constant, $c(NH_3)$ is ammonia concentration, V is the volume

of electrolyte, *t* is the reaction time and *m* is the catalyst mass.

The electrochemical specific surface area (ECSA) of $V_3O_7{\cdot}H_2O$ monolith and $V_3O_7{\cdot}H_2O$ powder electrodes were obtained by CVs in a small potential range of 0.4-0.5 V (*vs.* RHE). The data was collected at different scan rates of 20, 40, 60, 80, 100, 120 mV s^{-1}. The plots of the $\Delta J = (J_a - J_c)$ (mA) at 0.45 V (*vs.* RHE) against the scan rate are nearly linear and the double layer capacitance (C_{dl} (mF)) is obtained. The ECSA value of various electrodes can be evaluated by the following formula:

$$\text{ECSA} = C_{dl} / C_s$$

Where C_s = 0.035 mF cm^{-2} (benchmark value, Joule 2019, 3, 279-289). As shown in Fig. S26, the ECSA values of $V_3O_7{\cdot}H_2O$ monolith (87.14 cm^{-2}) is higher than that of $V_3O_7{\cdot}H_2O$ powder (42.57 cm^{-2}).

Electrochemical impedance spectroscopy (EIS) for $V_3O_7{\cdot}H_2O$ monolith and $V_3O_7{\cdot}H_2O$ powder was tested in open circuit with the frequency ranging from 10^5 to 0.01 Hz.

Determination of NH_3 by indophenol blue method. Preparation of chromogenic reagents: 2 mL of 1 M NaOH solution was dissolved in 5 wt% of sodium citrate and 5 wt% of salicylic acid to make solution A; 1 mL of 0.05 M NaClO solution was labelled as B; 0.2 mL 1 wt% of $C_5FeN_6Na_2O$ aqueous solution was marked as C.

Preparation of the test solutions: After 2 hrs of NRR chronoamperometric test, cathode solution, anode solution and the first exhaust gas absorption liquid were collected. The corresponding membrane was soaked in 5 mL of 0.5 M sulfuric acid

for 24 hrs and diluted to 50 mL. All of these solutions were used as test solutions for determine NRR performances.

UV-Vis absorption spectrum measurement: 2 mL of test solutions were mixed with color reagents A, B and C in sequence. After 2 hrs in dark under ambient condition, the UV-Vis absorption spectrum was measured at 655 nm.

Determination of N_2H_4 by Watt and Chrisp method. A mixture solution of para-(dimethylamino) benzaldehyde (5.99 g), HCl (35%, 30 mL) and ethanol (300 mL) was used as a colour reagent. An equal amount of the color developing reagent was mixed with the test solutions for 30 minutes; and UV-Vis absorbance was measured at 455 nm.

$^{15}N_2$ isotope labelling experiment. An isotopic labelling experiment with $^{15}N_2$ enriched feeding gas can clarify the source of ammonia. Firstly, Ar gas was passed through the electrolytic cell for 30 minutes to remove the contamination in electrolytes. Next, NRR was carried out for 20 hrs (H-cell) and 6 hrs (Flow-cell) with $^{15}N_2$ feeding gas at the gas flow of 20 mL min^{-1}. The reaction electrolyte was then adjusted to pH=2 and concentrated for ^1H nuclear magnetic resonance (NMR, 500 MHz) spectrometer analyses.

4. Theoretical simulations. Computations were conducted by using density functional theory (DFT) with spin polarization. The ionic cores were illustrated by the projector-augmented wave (PAW) method. The Perdew-Burke-Ernzerhof (PBE) functional in combination with DFT approach was used for electron exchange-correlation within the generalized gradient approximation (GGA)

implemented in VASP package code. The cut-off energy for plane wave expansion was fixed at 400 eV, optimized from a range of cut-off energies. The electronic self-consistent-loop criterion was set to 10^{-4} eV. During geometry optimization, the structures were relaxed to forces on all atoms smaller than 0.05 eV/Å. A Gaussian smearing method was employed with 0.10 eV width. The K-points for structural optimization in all models were set to 1 × 2 × 3.

According to XRD and XPS results, the structural model is built by $V_3O_7{\cdot}H_2O$ (200) surface cleaved across a crystal direction that form a slab with (2×2) unit cell based on Pnam space group. Different adsorption sites of for H* and HNN* were investigated for studying the mechanism of NRR. During optimization of adsorption mediates, the bottom layer of substrate atoms was fixed to allow a time-efficient relaxation of the adsorbed species. The detailed Gibbs free energy calculation for NRR has been carried out as it follows:

$$G=E+\int C_P dT-TS \quad (4)$$

where G, E and C_P refer to the chemical potential (partial molar Gibbs free energy), electronic energy and heat capacity, respectively. The entropy term can be expressed as the sum of the translational, rotational, vibrational and electronic contributions as to:

$$S=S_t+S_r+S_v+S_e \quad (5)$$

And finally, intrinsic zero-point energy (ZPE) and extrinsic dispersion (D) corrections can be included to finally obtain:

$$G=E+\int C_P dT-T(S_t+S_r+S_v+S_e)+ZPE+D \quad (6)$$

Since $S_e \approx 0$ at the fundamental electronic level.

For the case of solids and adsorbates, some approximations can be assumed:

1. As for gases, at the fundamental electronic level $S_e \approx 0$.

2. Translational and rotational motions can be neglected, therefore, $S_t \approx 0$ and $S_r \approx 0$.

In this sense, all entropy contributions come from vibrations: $S = S_v$. Similarly, translational and rotational contributions to the heat capacity are neglected.

Therefore, Gibbs free energies for the different states have been calculated as to:

$$G=E+\int C_P dT - TS_v + ZPE + D \quad (7)$$

II. Supplementary Results

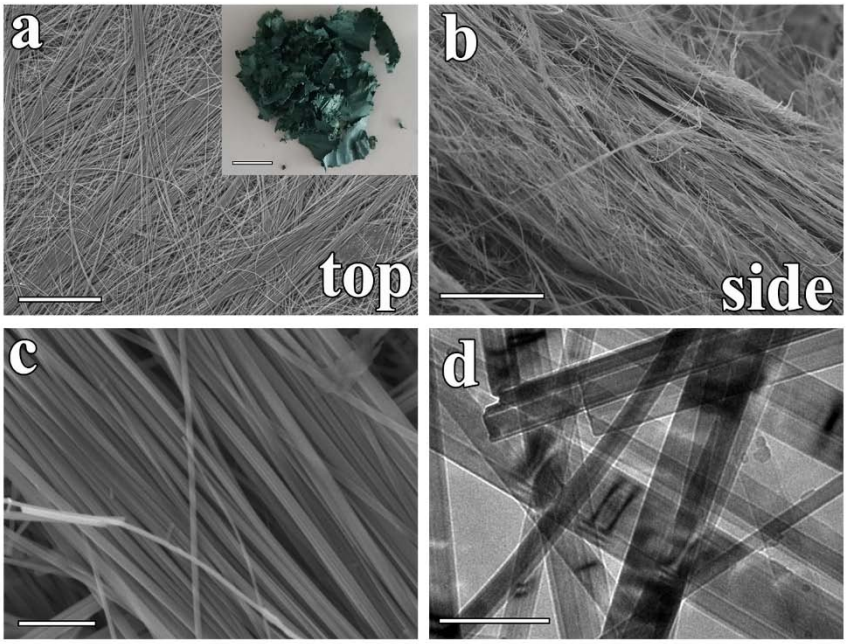

Fig. S1. a-c) SEM image of $V_3O_7{\cdot}H_2O$ powder (scale bars are 20 μm, 30 μm, and 1 μm for a, b and c). The inset of (a) is an optical image (scale bars: 1 cm). d) TEM images (scale bars: 200 nm).

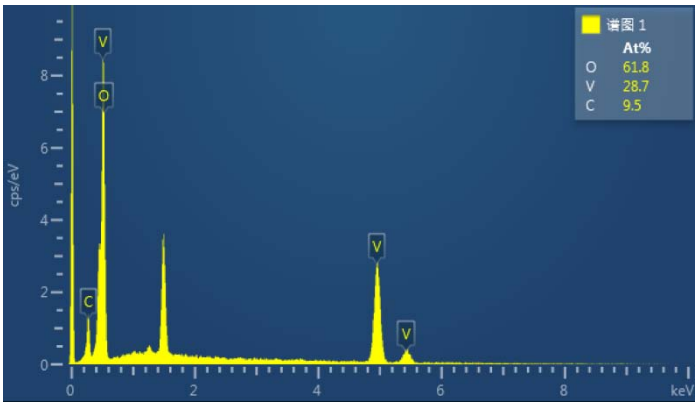

Fig. S2. EDS data for $V_3O_7 \cdot H_2O$ powder.

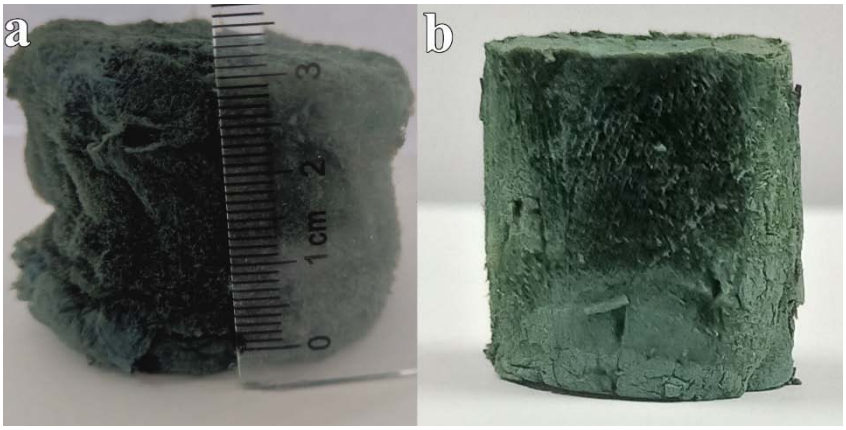

Fig. S3. High-resolution optical image of $V_3O_7 \cdot H_2O$ monolith with the concentration of (a) 0.75 mg mL^{-1} and (b) 4.8 mg mL^{-1}.

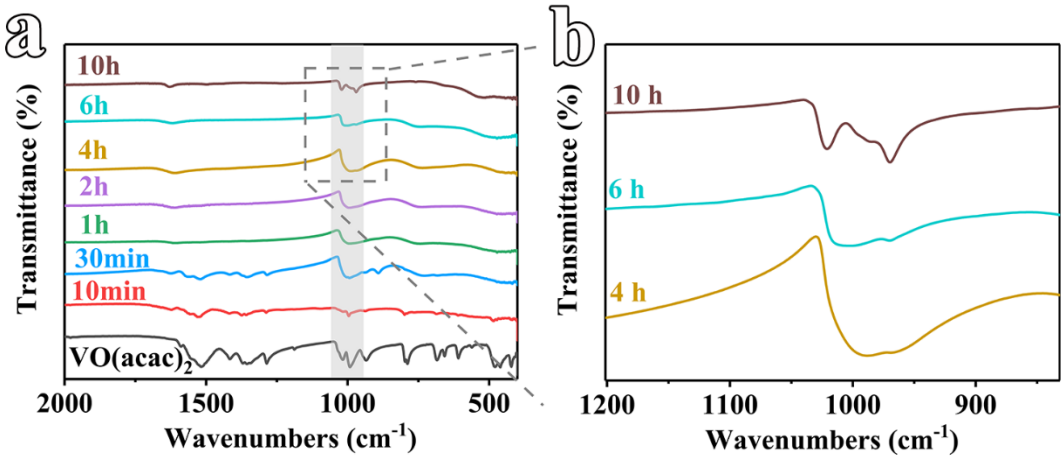

Fig. S4. Infrared spectra (FT-IR) of reaction intermediates for $V_3O_7{\cdot}H_2O$ at different reaction durations.

Supplementary Note. At 30 min, most characteristic vibration peaks of VO $(acac)_2$ disappear, indicating the completion of hydrolysis process. At 4-6 hrs, the characteristic peak of V=O double begins to split into a double peak of V^{+5}=O (1018 cm^{-1}) and V^{+4}=O (969 cm^{-1}) for $V_3O_7{\cdot}H_2O$. At 10 hrs, the reaction was almost completed by showing stable characteristic peaks for $V_3O_7{\cdot}H_2O$. Further increase of the reaction duration show little change in structure.

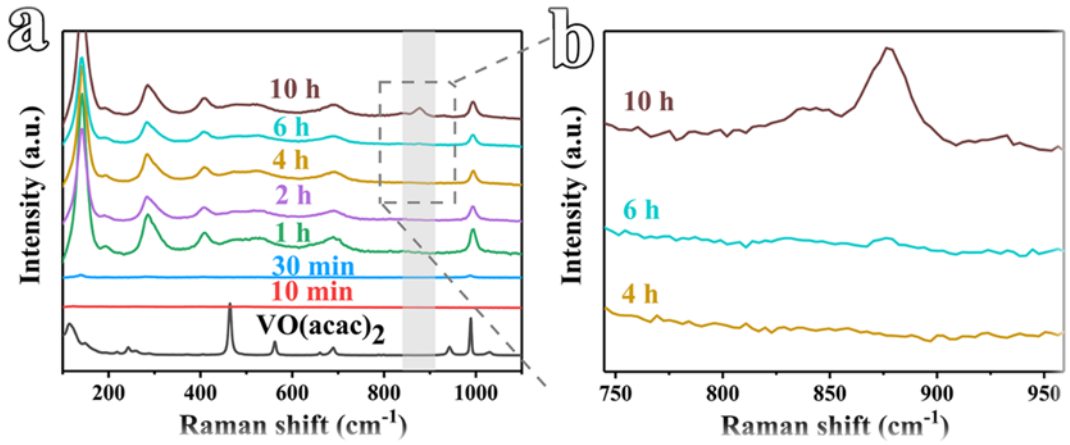

Fig. S5. Raman spectra of reaction intermediates for $V_3O_7 \cdot H_2O$ at different reaction durations, which shows the formation of characteristic edge-sharing and corner-sharing V-O bonds (874 cm^{-1}) for $V_3O_7 \cdot H_2O$ structure after 10 hrs, indicating the crystal growth process completed after that duration.

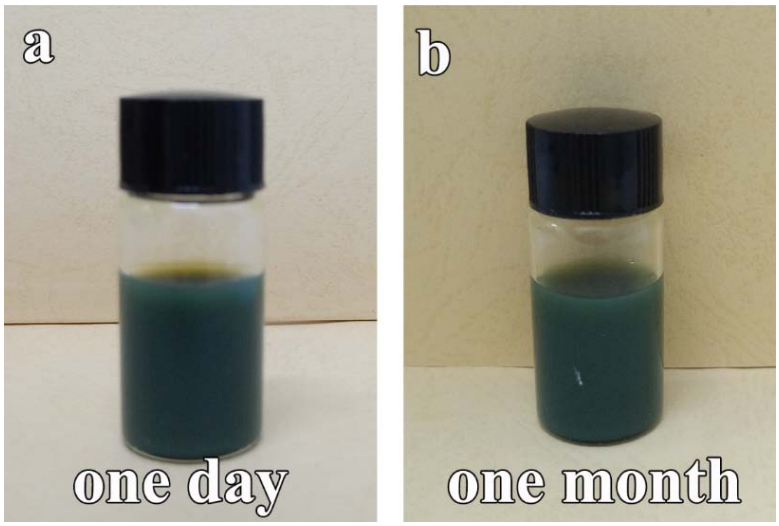

Fig. S6. Optical photographs of $V_3O_7 \cdot H_2O$ aqueous dispersion at different durations.

a

		Mean (mV)	Area (%)	St Dev (mV)
Zeta Potential (mV): -30.3	Peak 1:	-30.3	100.0	8.56
Zeta Deviation (mV): 8.56	Peak 2:	0.00	0.0	0.00
Conductivity (mS/cm): 0.00609	Peak 3:	0.00	0.0	0.00

Result quality : Good

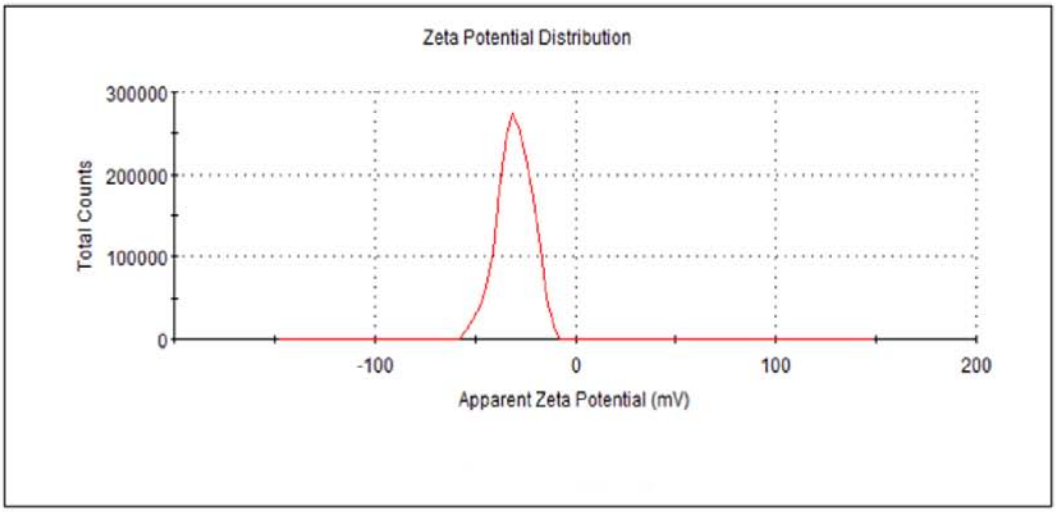

b

		Mean (mV)	Area (%)	St Dev (mV)
Zeta Potential (mV): -29.4	Peak 1:	-29.4	100.0	8.21
Zeta Deviation (mV): 8.21	Peak 2:	0.00	0.0	0.00
Conductivity (mS/cm): 0.00605	Peak 3:	0.00	0.0	0.00

Result quality : Good

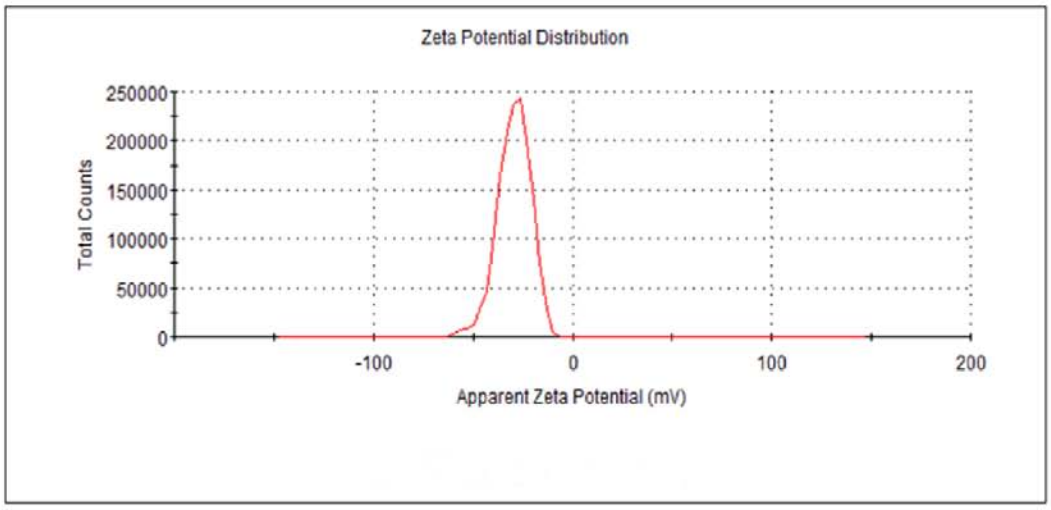

Fig. S7. The zeta potential of $V_3O_7 \cdot H_2O$ aqueous dispersion at different durations. a) one day. b) one month.

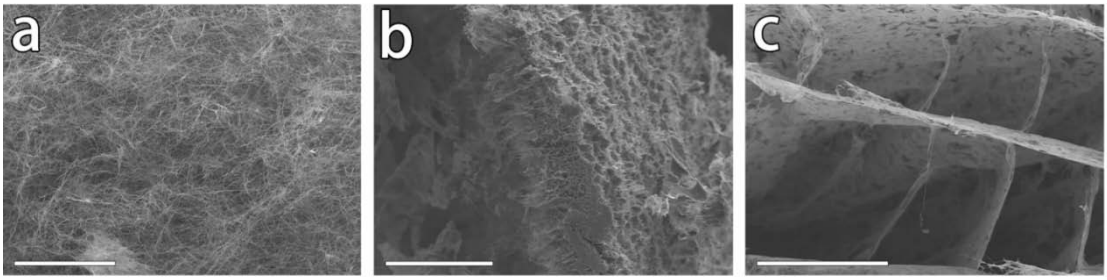

Fig. S8. SEM images of $V_3O_7 \cdot H_2O$ monolith obtained by different freezing methods. a) liquid nitrogen added quickly. b) refrigerator. c) liquid nitrogen added slowly. Scale bars: 100 μm.

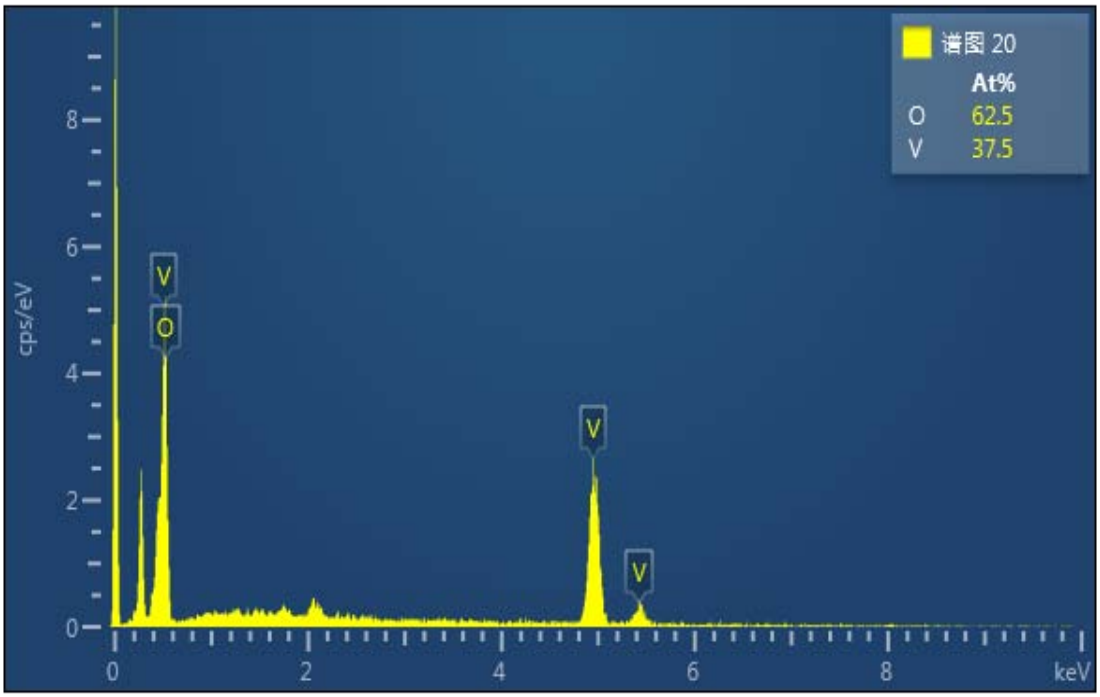

Fig. S9. SEM EDS data of $V_3O_7 \cdot H_2O$ monolith.

Supplementary Note for Fig. 2b in the main text. The FT-IR of $V_3O_7 \cdot H_2O$ monolith and $V_3O_7 \cdot H_2O$ powder is shown in Fig. 2b. The peaks at 1018 cm^{-1}, 969 cm^{-1}, and 535 cm^{-1} are attributed to the characteristics of the V-O vibration band. The band at 1018 cm^{-1} and 969 cm^{-1} is attributed to the tensile vibration of V^{5+}=O and V^{4+}=O, respectively, and the band at 535 cm^{-1} corresponds to the symmetric stretching vibrations of the V-O-V bridge. At the same time, two typical bands of about 3394 cm^{-1} and 1628 cm^{-1} represent O-H stretching and H-O-H bending vibration modes. It is shown that the sample consists of valence vanadium atoms and water.

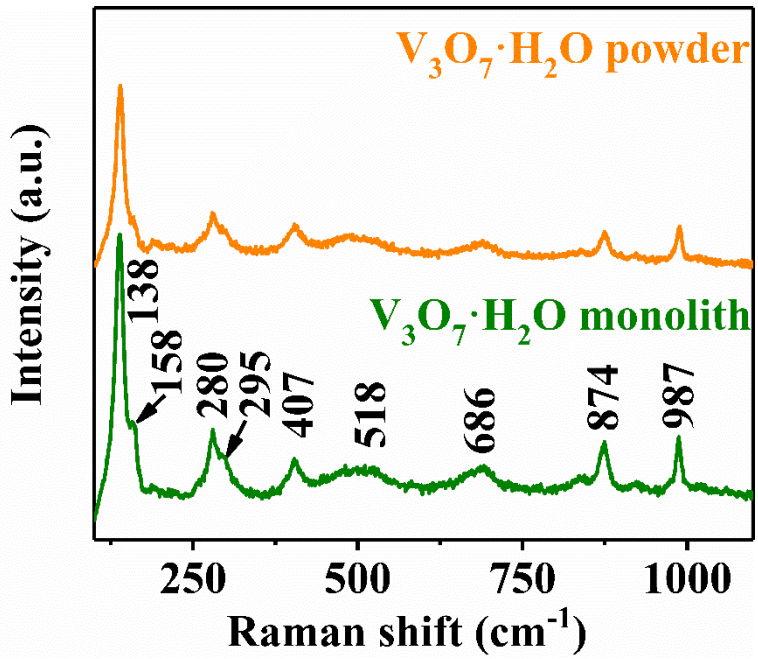

Fig. S10. Raman spectra of $V_3O_7 \cdot H_2O$ monolith and powder.

Supplementary Note. Fig. S10 shows the Raman spectra of $V_3O_7 \cdot H_2O$ monolith and $V_3O_7 \cdot H_2O$ powder. The low frequency peaks at 138 cm^{-1} and 158 cm^{-1} are assigned to the chain translation associated with the hierarchy. The peaks at 280 cm^{-1}, 295 cm^{-1}, and 407 cm^{-1} are attributed to the bending vibration of V-O, and the three peaks at 518 cm^{-1}, 686 cm^{-1}, and 874 cm^{-1} are related to the V-O tensile vibration, where 874 cm^{-1} is considered a xerogel pattern with edge-sharing V-O bonds and corner-sharing V-O bonds. The peak at 987 cm^{-1} is attributed to the end V=O tensile vibration.

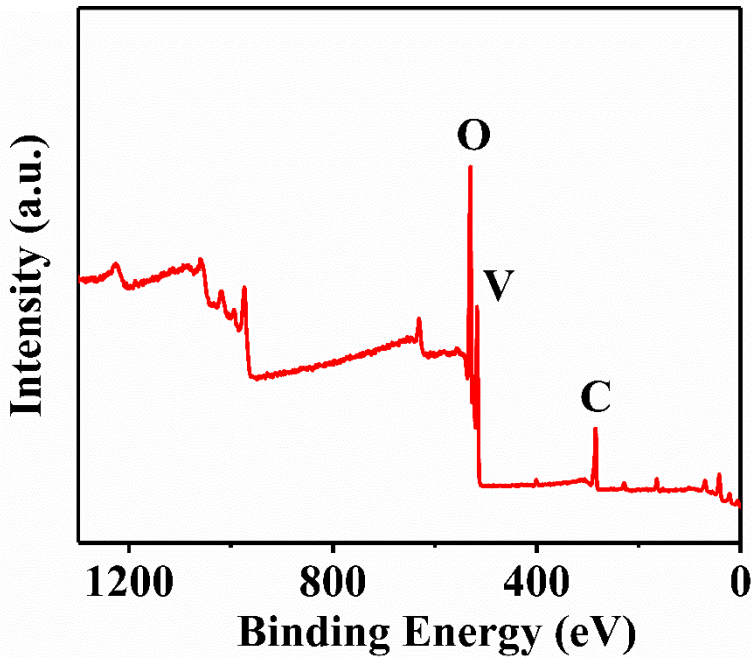

Fig. S11. XPS spectra of $V_3O_7 \cdot H_2O$ monolith.

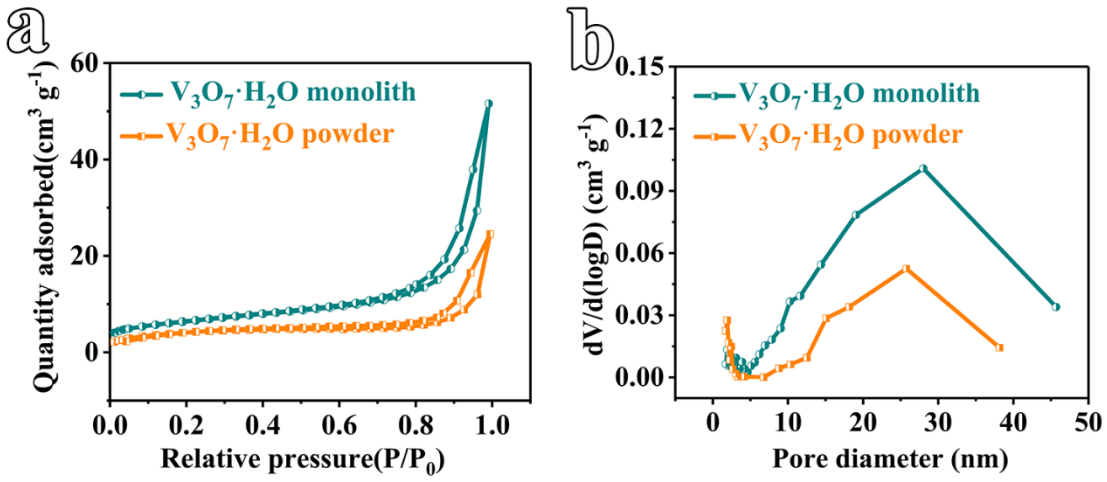

Fig. S12. a) N_2 adsorption-desorption isotherms of the $V_3O_7{\cdot}H_2O$ monolith and powder. b) shows corresponding BJH pore size distributions.

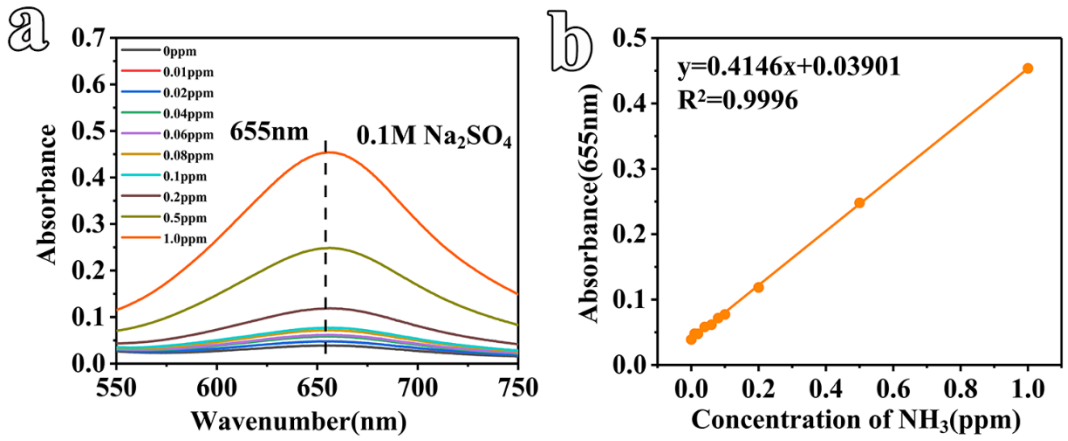

Fig. S13. Calibration curve of ammonium chloride solution in 0.1 M Na_2SO_4 solution. a) UV-Vis absorption spectra. b) calibration curve.

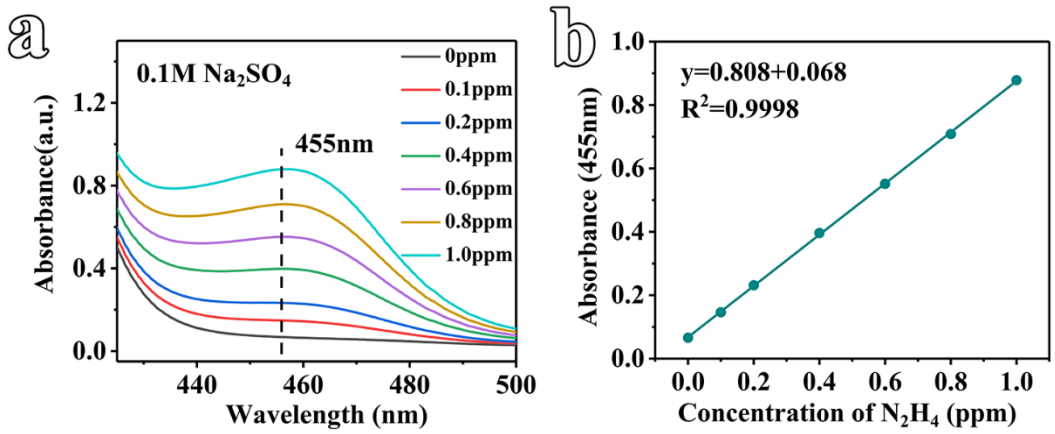

Fig. S14. Calibration curve of N_2H_4 solution in 0.1 M Na_2SO_4 solution. a) UV-Vis absorption spectra of Watt and Chrisp methods. b) calibration curve.

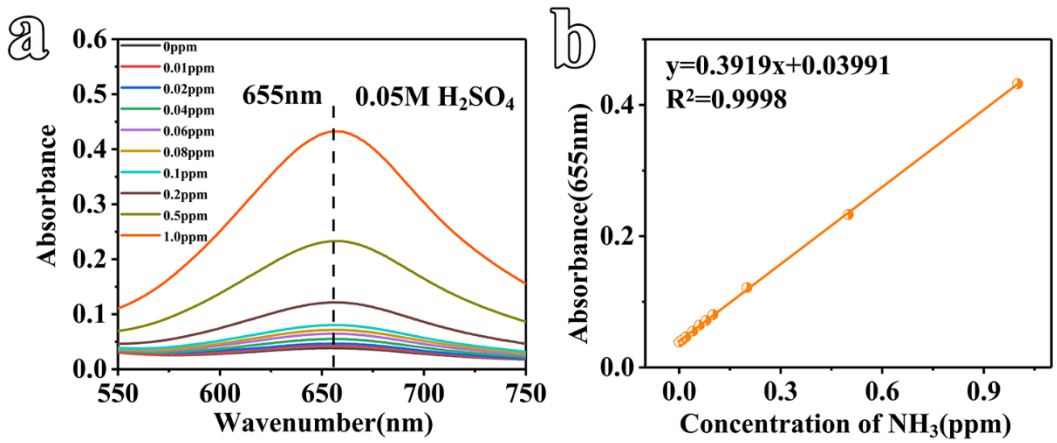

Fig. S15. Calibration curve of ammonium chloride solution in 0.05 M H_2SO_4 solution. a) UV-Vis absorption spectra of indophenol assays. b) calibration curve.

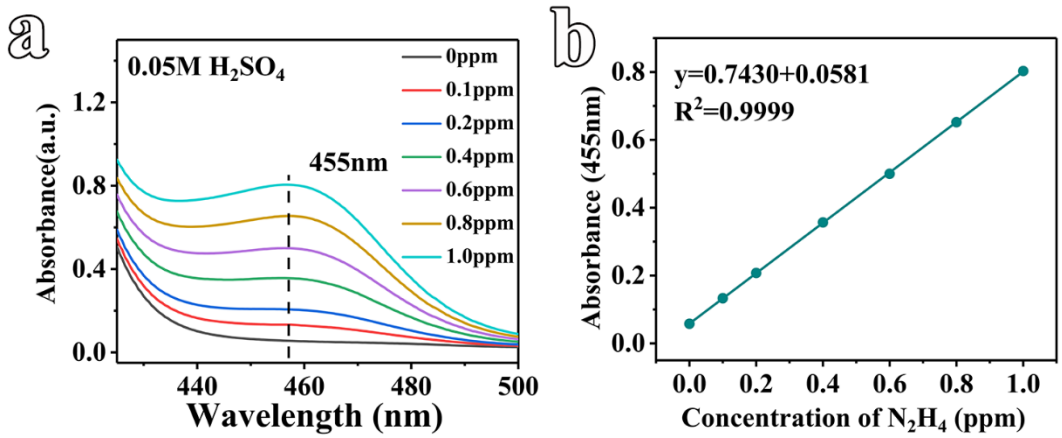

Fig. S16. Calibration curve of N_2H_4 solution in 0.05 M H_2SO_4 solution. a) UV-Vis absorption spectra of Watt and Chrisp methods. b) calibration curve.

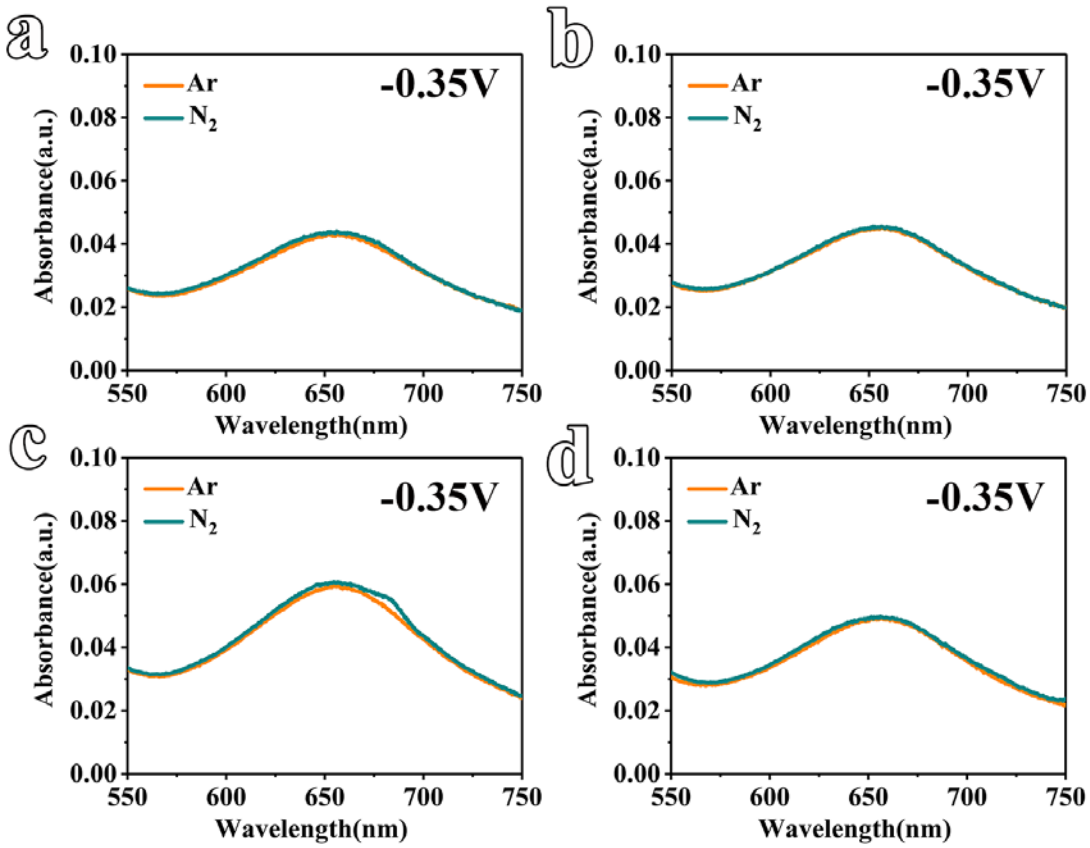

Fig. S17. The UV absorption spectrum of $V_3O_7{\cdot}H_2O$ monolith electrode after continuous testing for 2 hrs at **-0.35 V (*vs.* RHE)** and N_2-saturated 0.1 M Na_2SO_4 solution. Where (a), (b), (c) and (d) are the cathode chamber, anode chamber, membrane, and exhaust gas absorption chamber, respectively.

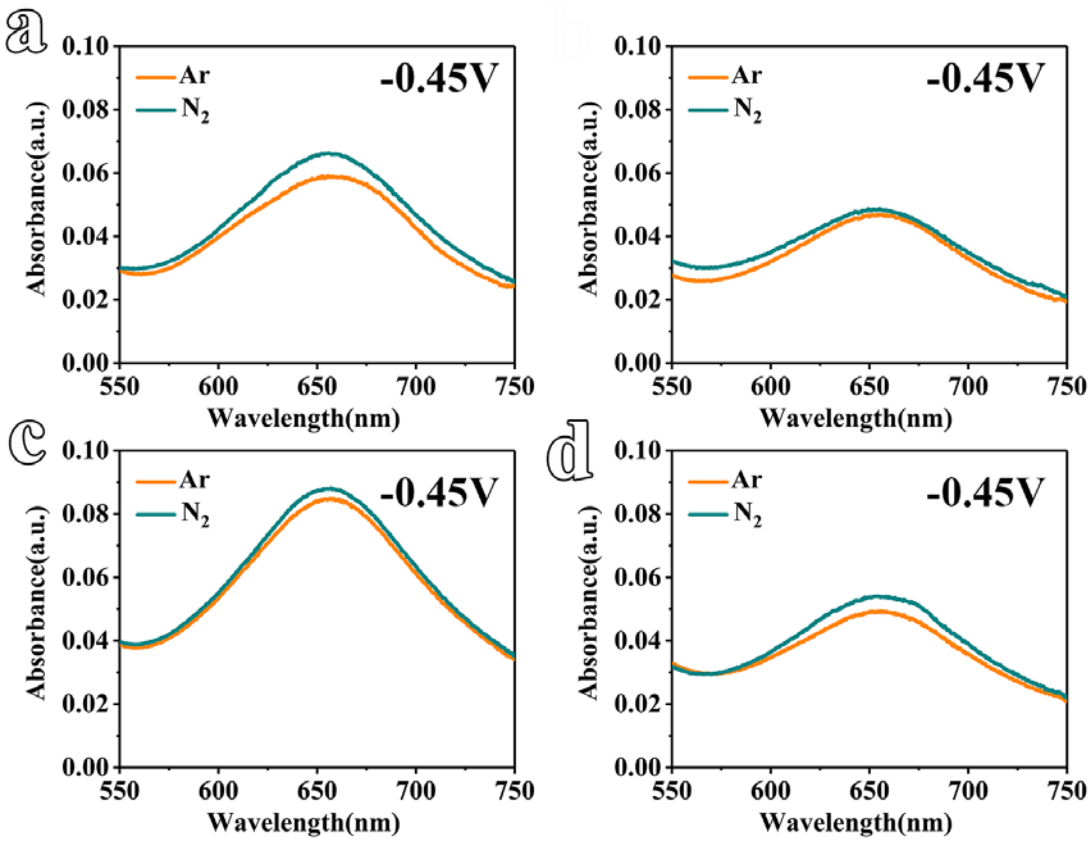

Fig. S18. The UV absorption spectrum of the $V_3O_7{\cdot}H_2O$ monolith electrode after continuous testing for 2 hrs at **-0.45 V (*vs.* RHE)** and N_2-saturated 0.1 M Na_2SO_4 solution. Where (a), (b), (c) and (d) are the cathode chamber, anode chamber, membrane, and exhaust gas absorption chamber, respectively.

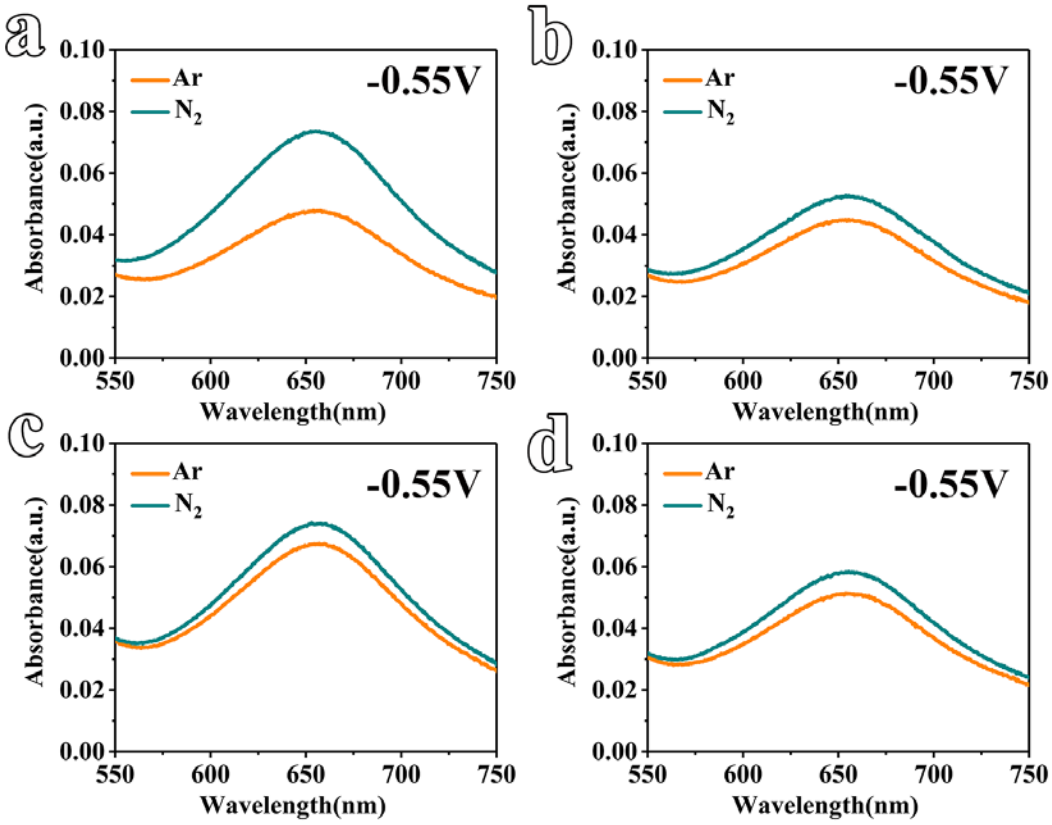

Fig. S19. The UV absorption spectrum of the $V_3O_7{\cdot}H_2O$ monolith electrode after continuous testing for 2 hrs at **-0.55 V (*vs.* RHE)** and N_2-saturated 0.1 M Na_2SO_4 solution. Where (a), (b), (c) and (d) are the cathode chamber, anode chamber, membrane, and exhaust gas absorption chamber, respectively.

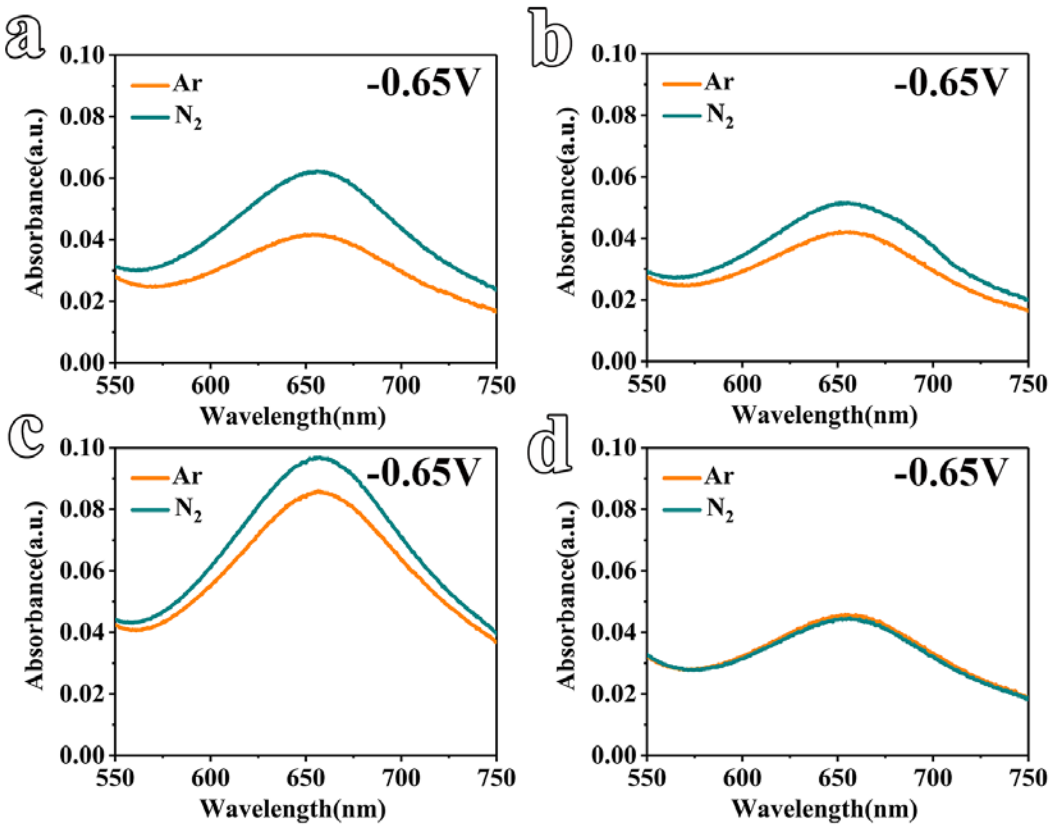

Fig. S20. The UV absorption spectrum of the $V_3O_7{\cdot}H_2O$ monolith electrode after continuous testing for 2 hrs at **-0.65 V (*vs.* RHE)** and N_2-saturated 0.1 M Na_2SO_4 solution. Where (a), (b), (c) and (d) are the cathode chamber, anode chamber, membrane, and exhaust gas absorption chamber, respectively.

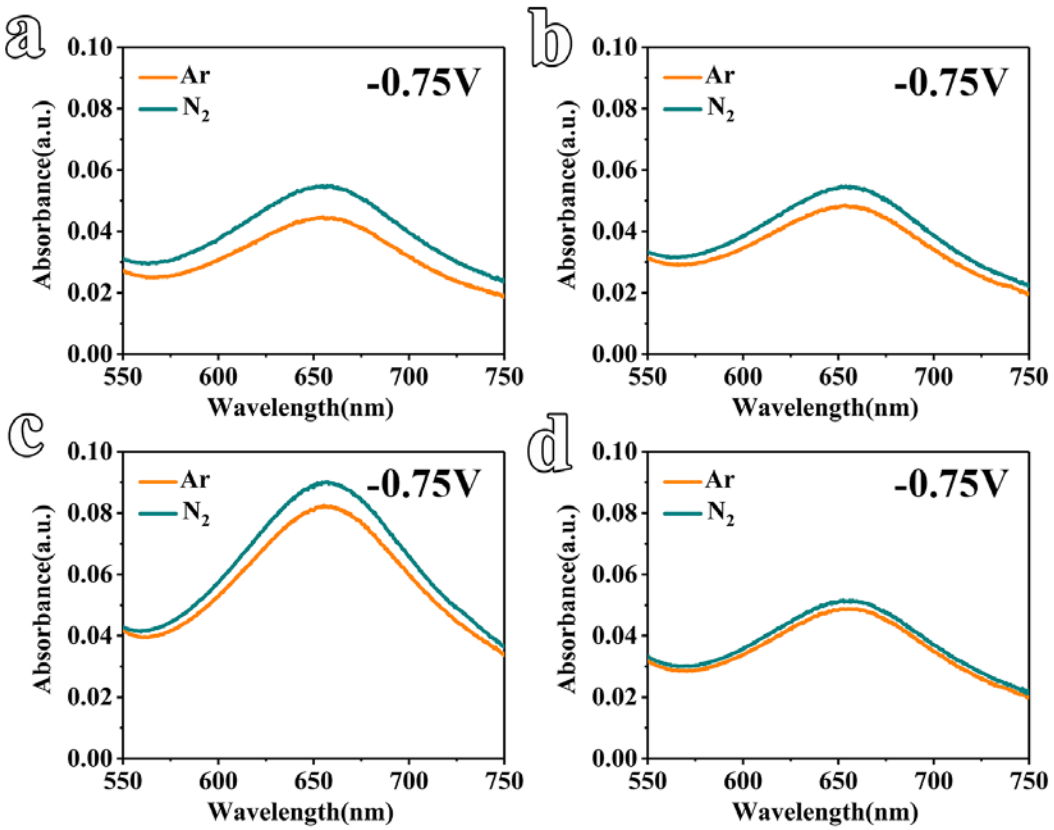

Fig. S21. The UV absorption spectrum of the $V_3O_7{\cdot}H_2O$ monolith electrode after continuous testing for 2 hrs at **-0.75 V (*vs.* RHE)** and N_2-saturated 0.1 M Na_2SO_4 solution. Where (a), (b), (c) and (d) are the cathode chamber, anode chamber, membrane, and exhaust gas absorption chamber, respectively.

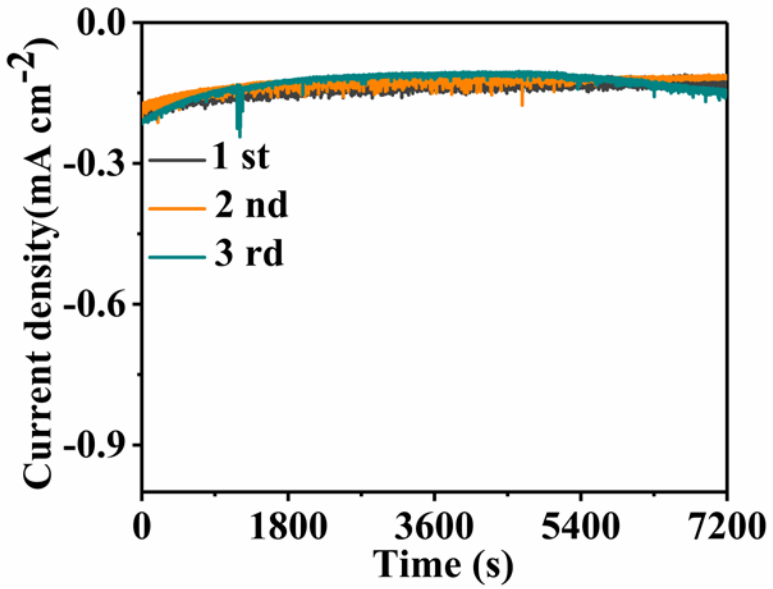

Fig. S22. Additional chronoamperometry curves of $V_3O_7{\cdot}H_2O$ monolith at -0.55 V (*vs.* RHE) in N_2-saturated 0.1 M Na_2SO_4 solution for 3 cycles to calculate the error bar in FE and NH_3 yield rate.

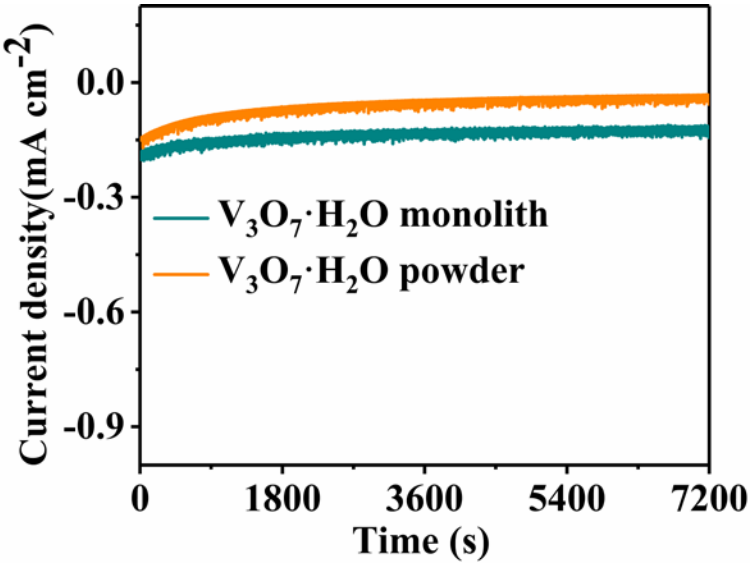

Fig. S23. Chronoamperometry curves of $V_3O_7{\cdot}H_2O$ monolith and powder at -0.55 V (*vs.* RHE) in N_2-saturated 0.1 M Na_2SO_4 solution.

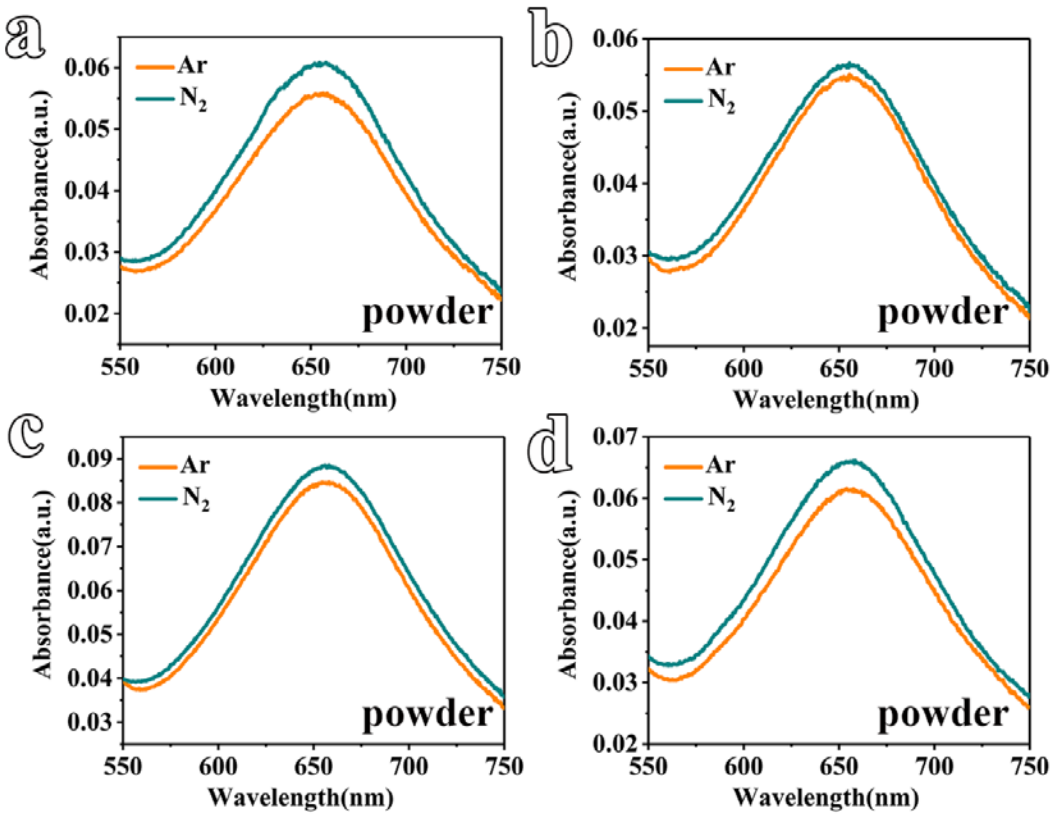

Fig. S24. The UV absorption spectrum of the $V_3O_7{\cdot}H_2O$ powder electrode after continuous testing for 2 hrs at **-0.55 V (*vs.* RHE)** and N_2-saturated 0.1 M Na_2SO_4 solution. Where (a), (b), (c) and (d) are the cathode chamber, anode chamber, membrane, and exhaust gas absorption chamber, respectively.

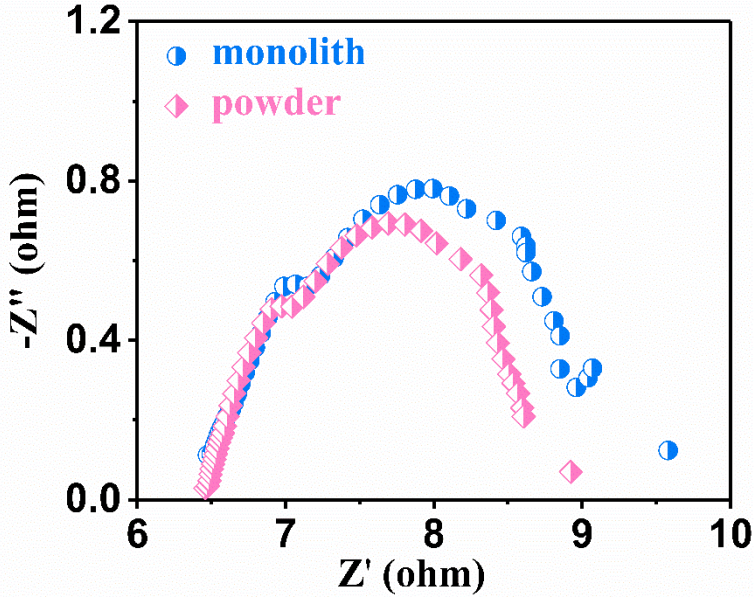

Fig. S25. EIS curves for $V_3O_7{\cdot}H_2O$ monolith and powder. According to Fig. S25, the solution resistance (Rs) of $V_3O_7{\cdot}H_2O$ monolith is 6.5 ohm (Ω), which is consistent to $V_3O_7{\cdot}H_2O$ powder (6.5 Ω). In addition, $V_3O_7{\cdot}H_2O$ monolith shows a semicircle comparable to $V_3O_7{\cdot}H_2O$ powder in the Nyquist diagram, indicating the similar R_{ct} for these electrodes (3.1 *vs*. 2.5 Ω).

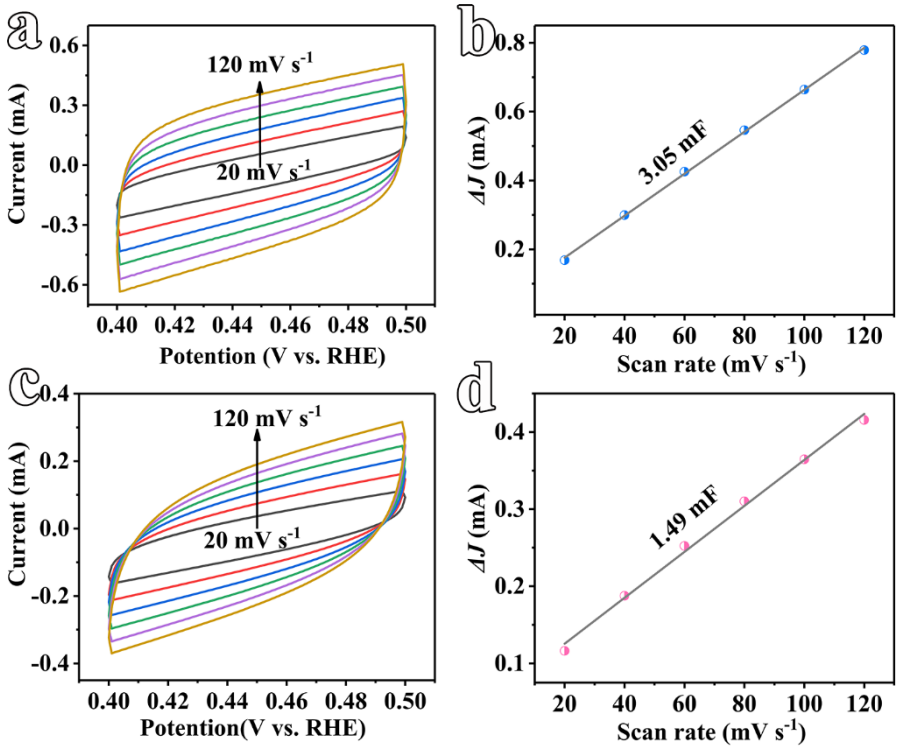

Fig. S26. ECSA data for $V_3O_7{\cdot}H_2O$ monolith and powders. Typical cyclic voltammetry curves of $V_3O_7{\cdot}H_2O$ monolith (a, b) and $V_3O_7{\cdot}H_2O$ powder (c, d). (a, c) the corresponding CVs measured at different scan rates from 20 to 120 mV s^{-1} in a potential region of 0.4-0.5 V (*vs.* RHE); (b, d) the $\Delta J = (Ja - Jc)$ at 0.45 V (*vs.* RHE) was plotted *vs.* scan rate, the slopes ($2C_{dl}$) were used to calculate the ECSA.

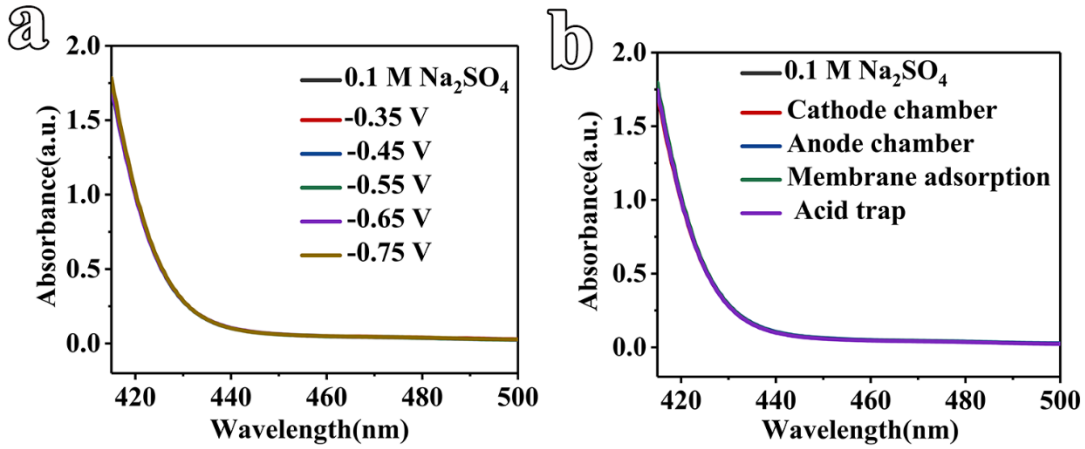

Fig. S27. Determine the possible hydrazine byproduct through Watt and Chrisp method. a) UV curves at different potentials. b) UV curves in different test sections at -0.55 V (*vs.* RHE).

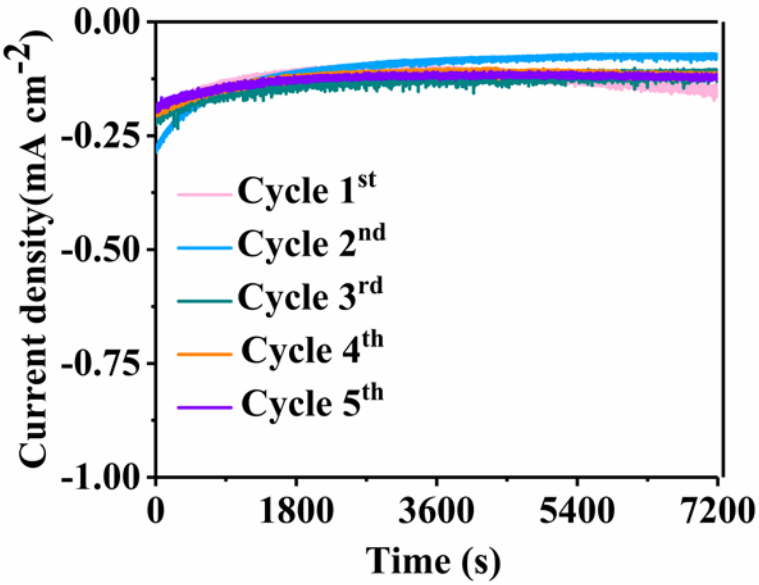

Fig. S28. Chronoamperometry curves of $V_3O_7 \cdot H_2O$ monolith at -0.55 V (*vs.* RHE) in N_2-saturated 0.1 M Na_2SO_4 solution for 5 cycles.

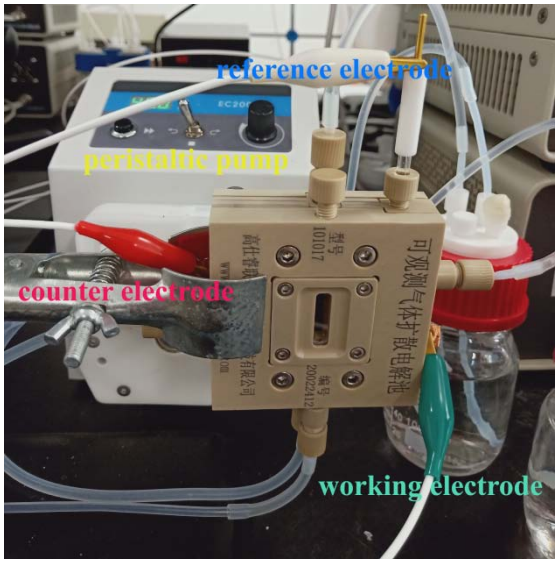

Fig. S29. An optical image of flow-type electrochemical cell for the electrocatalytic NRR to generate ammonia.

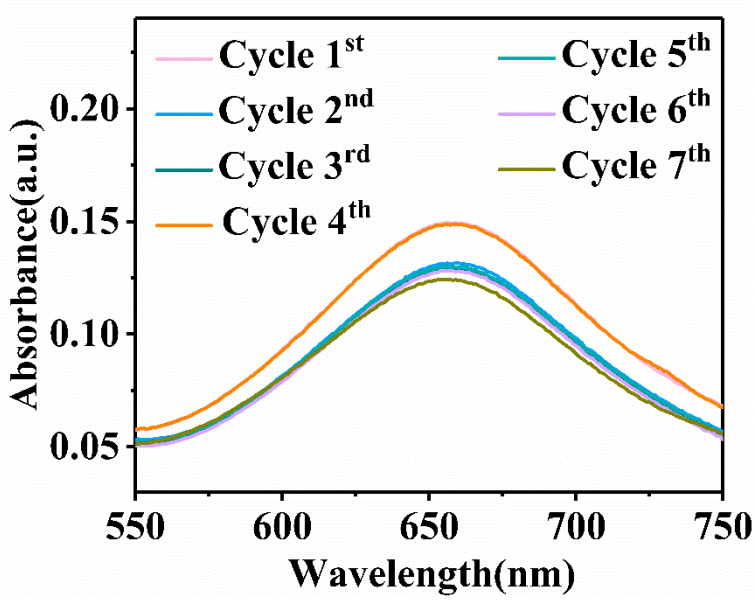

Fig. S30. The UV absorption spectrum of $V_3O_7 \cdot H_2O$ monolith-based electrode after continuous testing for 1 hr in a flow cell at -0.55 V (*vs.* RHE) for seven cycles.

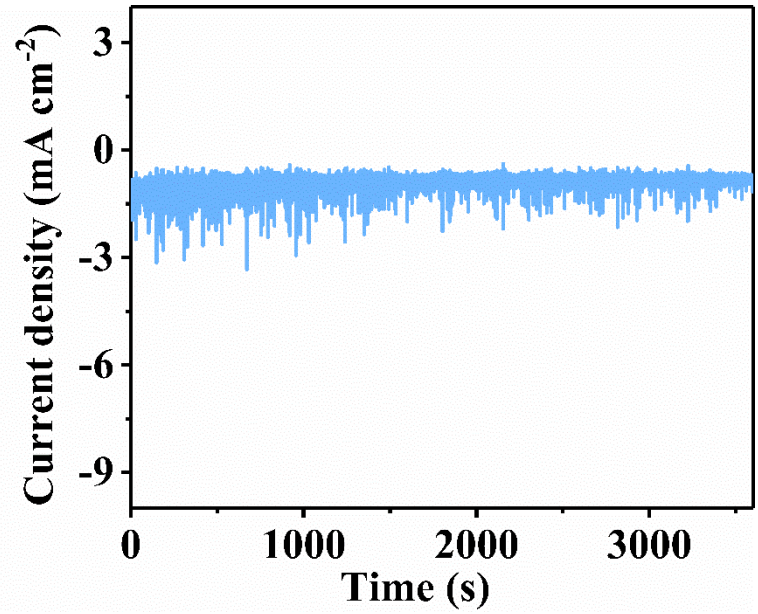

Fig. S31. Chronoamperometry curves of $V_3O_7 \cdot H_2O$ powder-based electrode at -0.55 V (*vs.* RHE) in N_2-saturated 0.1 M Na_2SO_4 solution in a flow cell.

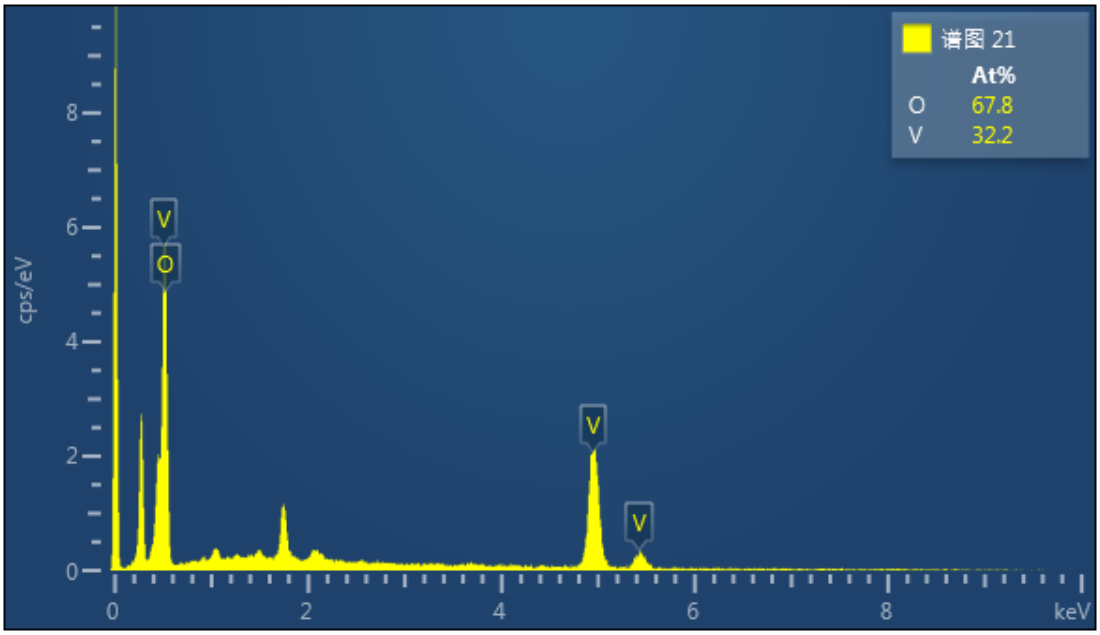

Fig. S32. SEM EDS data of $V_3O_7{\cdot}H_2O$ monolith-based electrode after stability test.

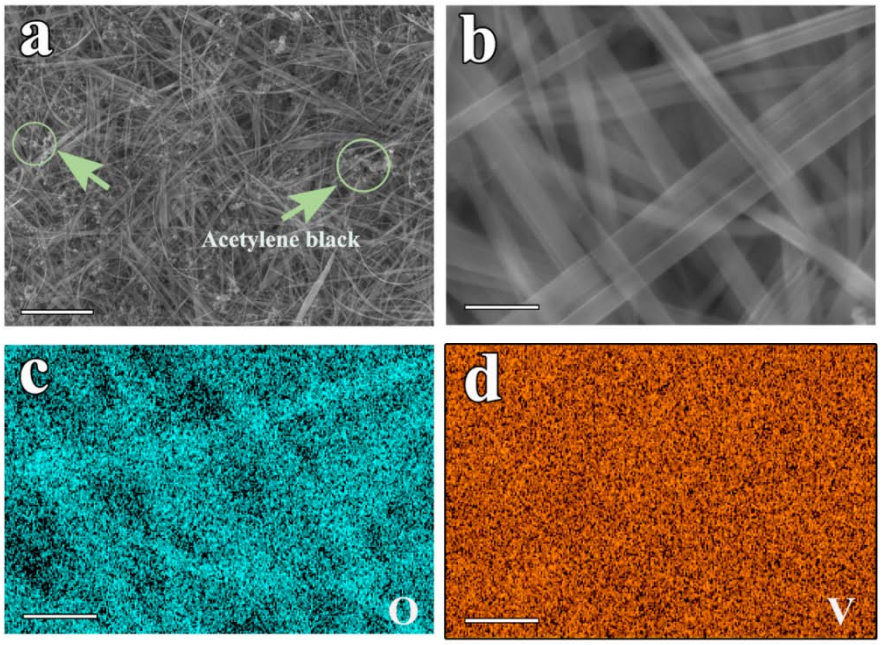

Fig. S33. Morphology of $V_3O_7 \cdot H_2O$ monolith-based electrode after stability test. a, b) SEM images (scale bars are 2 μm for a, 200 nm for b). c, d) SEM element mapping of O and V (scale bar, 200 nm).

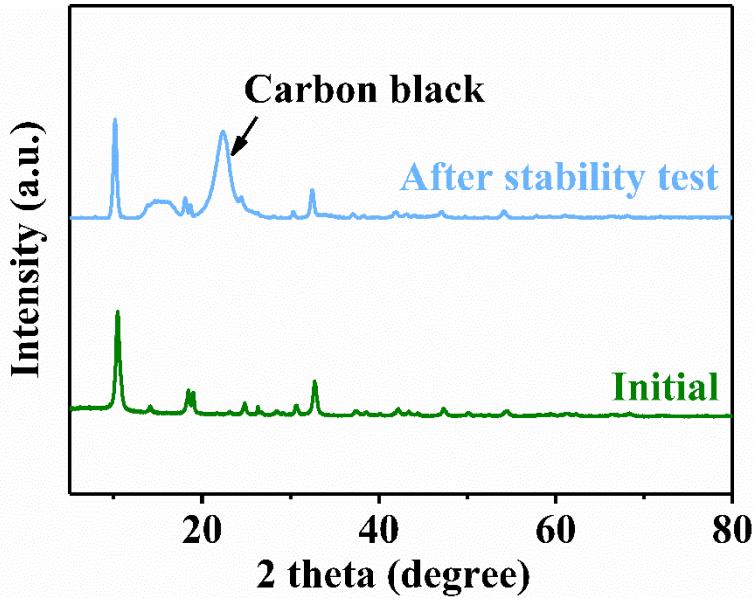

Fig. S34. XRD patterns of $V_3O_7 \cdot H_2O$ monolith-based electrode after stability test.

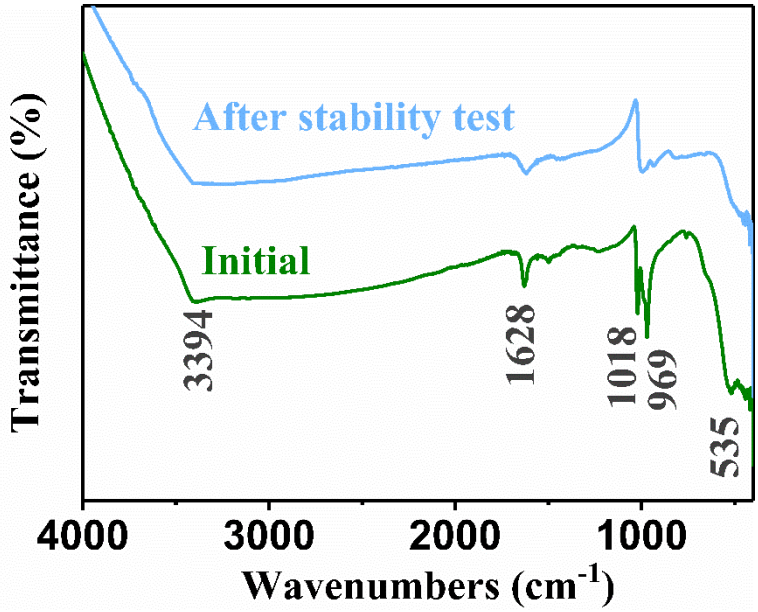

Fig. S35. FT-IR spectra of $V_3O_7 \cdot H_2O$ monolith-based electrode after stability test.

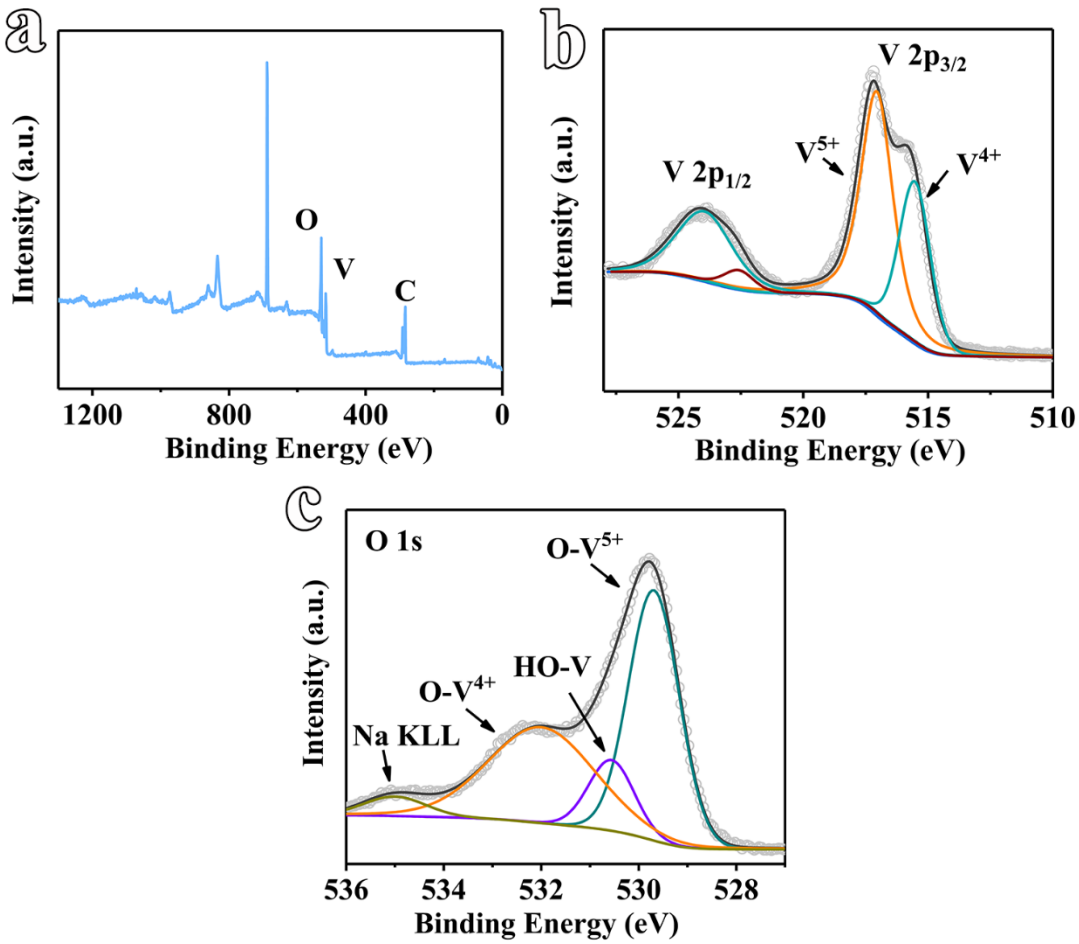

Fig. S36. XPS spectra of $V_3O_7{\cdot}H_2O$ monolith-based electrode after stability test. a) survey. b) V 2p. c) O1s.

Supplementary Note. The protrusion at 535 eV is the peak of Na Auger peak (Na KLL), which is attributed to the adsorption of Na_2SO_4 electrolyte on the surface of the electrode material.

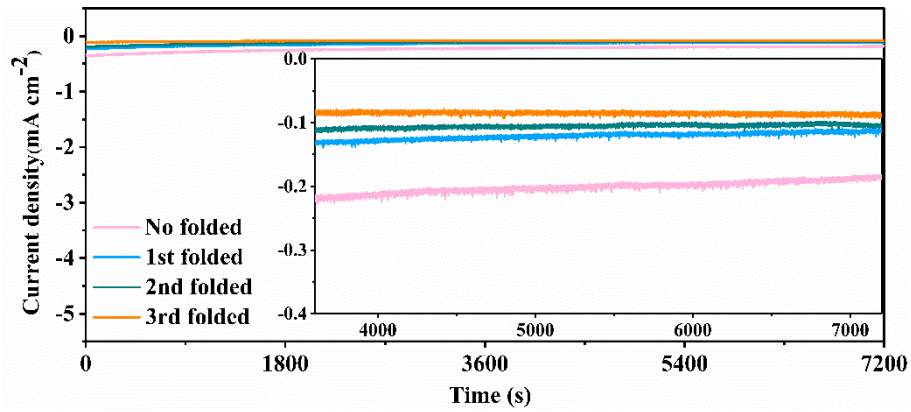

Fig. S37. Chronoamperometry curves of $V_3O_7 \cdot H_2O$ powder-based electrode at -0.55 V (*vs.* RHE) for different electrode foldings. The inset shows an enlarged area of the chronoamperometry curves.

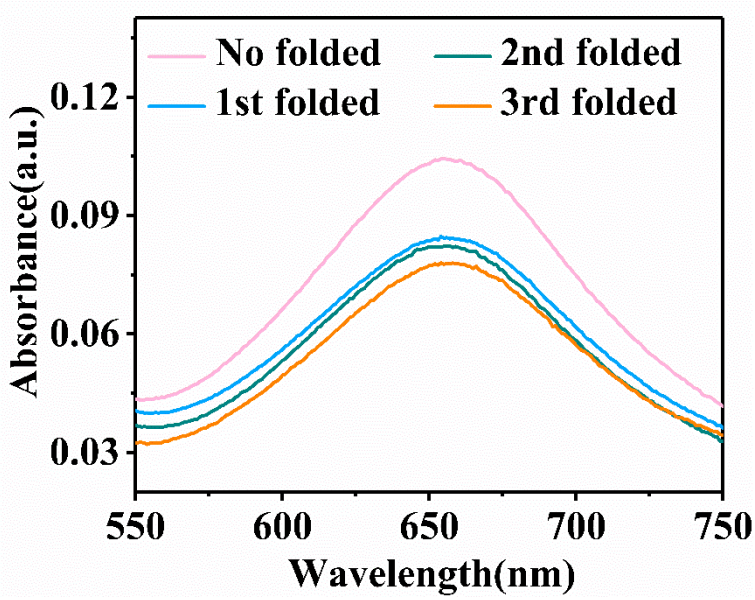

Fig. S38. The UV absorption spectrum of $V_3O_7 \cdot H_2O$ powder-based electrode at -0.55 V (*vs.* RHE) for different electrode foldings.

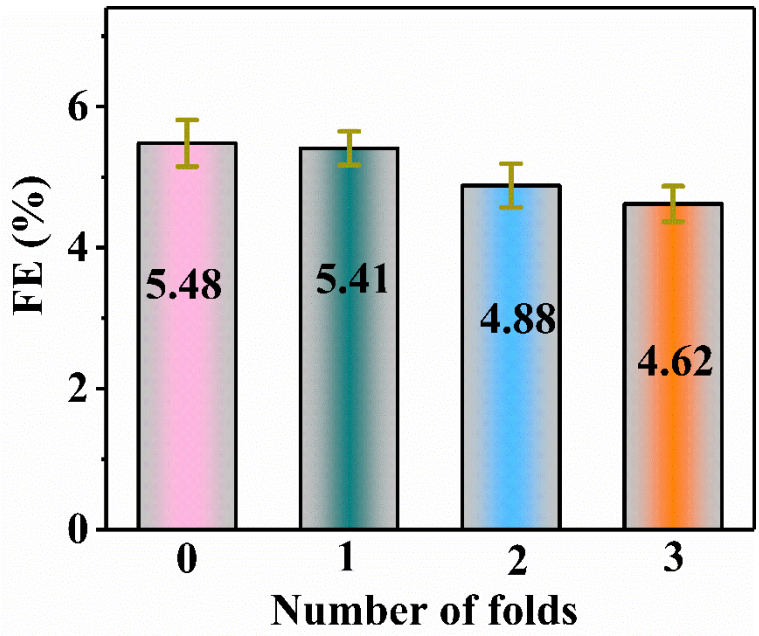

Fig. S39. The FEs of $V_3O_7{\cdot}H_2O$ powder-based electrode at -0.55 V (*vs.* RHE) for different electrode foldings.

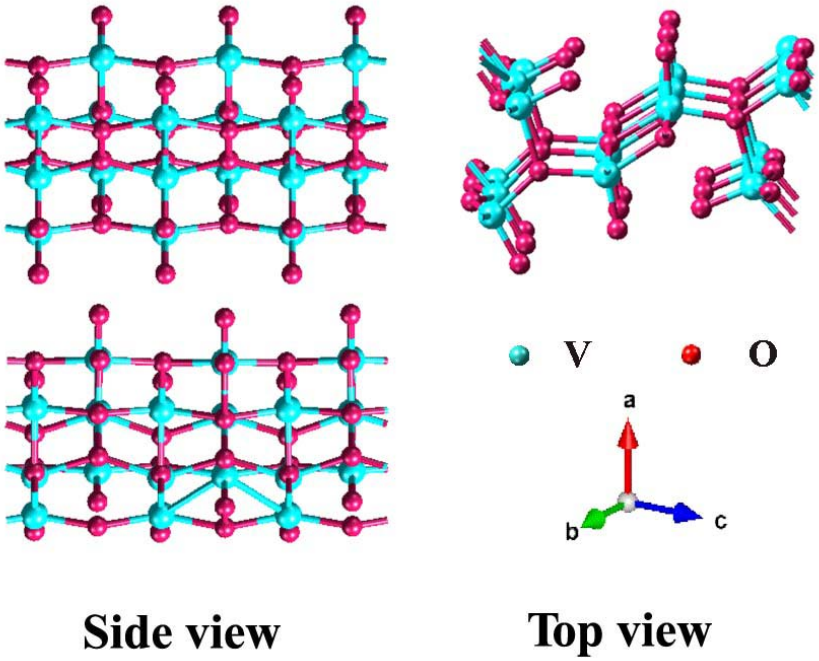

Fig. S40. Optimized structure for $V_3O_7 \cdot H_2O$ for DFT computation.

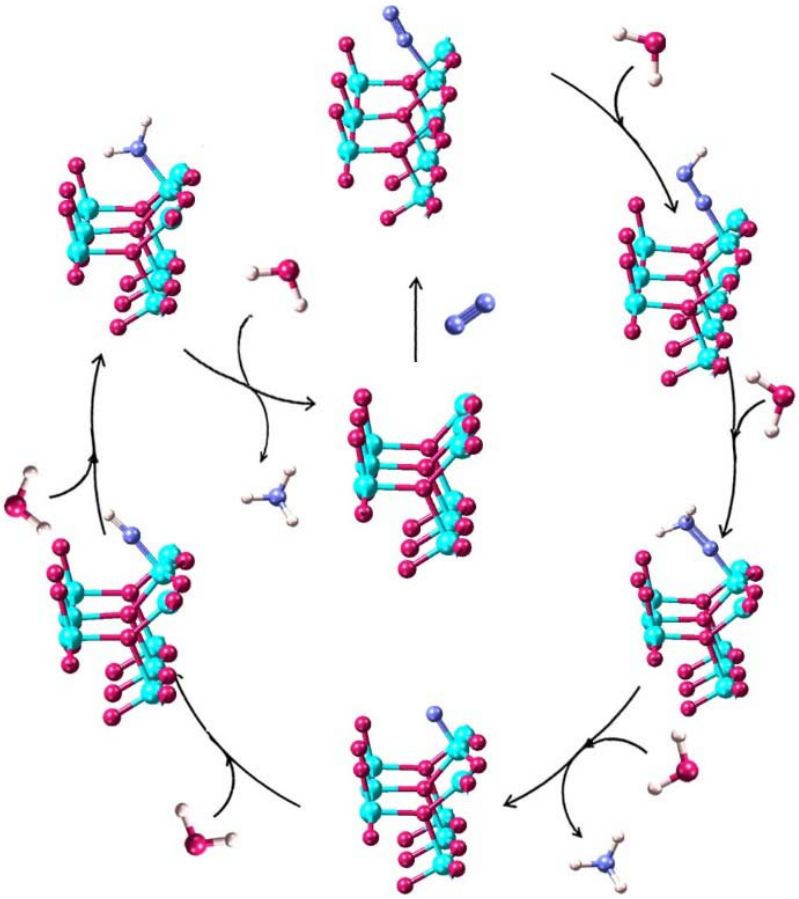

Fig. S41. NRR associative distal pathway at $V_3O_7{\cdot}H_2O$ for DFT computation.

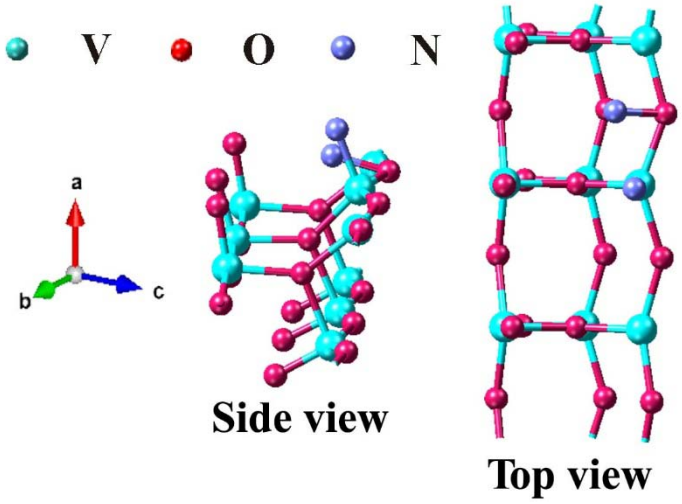

Fig. S42. NRR dissociative intermediate at $V_3O_7 \cdot H_2O$ for DFT computation.

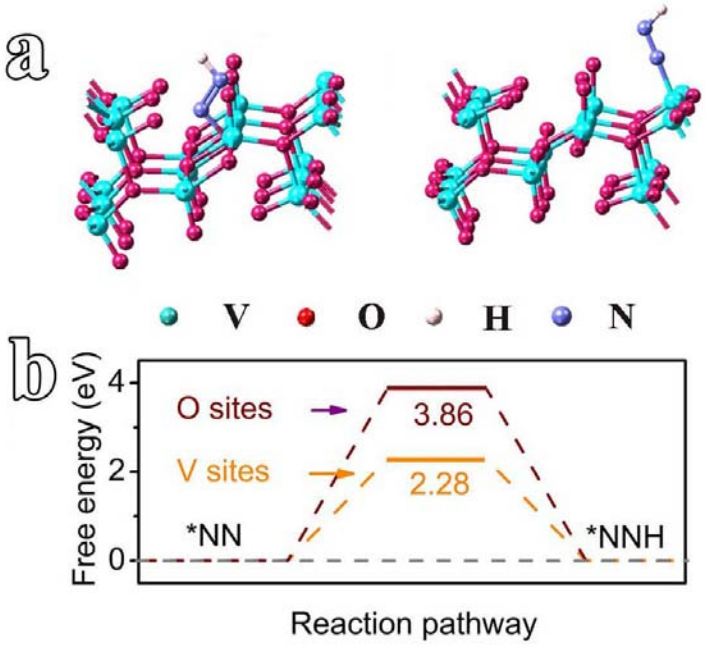

Fig. S43. Different NRR active sites of $V_3O_7{\cdot}H_2O$ for DFT computation.

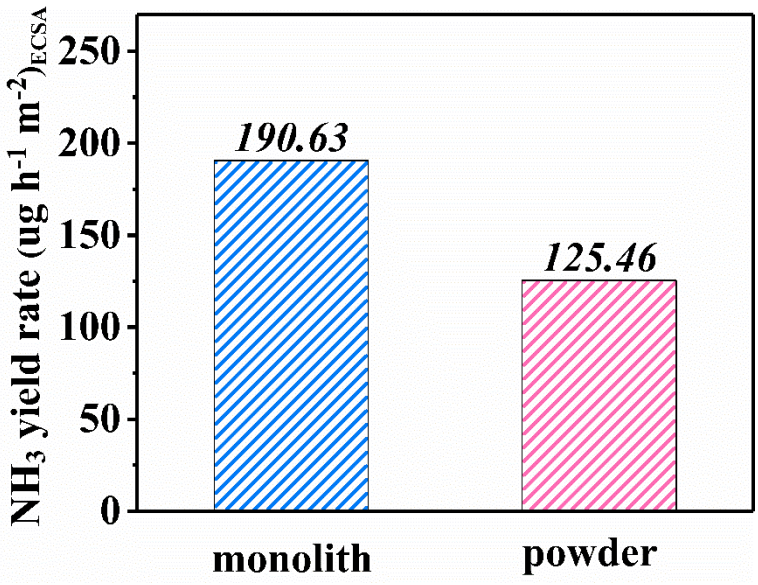

Fig. S44. NH_3 yield rates of $V_3O_7{\cdot}H_2O$ monolith and powders-based electrode normalized according to ECSA.

Table S1. The Brunauer-Emmett-Teller (BET) surface area of $V_3O_7 \cdot H_2O$ monolith and powder.

Sample	BET specific surface area /m^2 g^{-1}	BJH volume of pores / cm^3 g^{-1}
$V_3O_7 \cdot H_2O$ monolith	22.3	0.077
$V_3O_7 \cdot H_2O$ Powder	14.3	0.035

Table S2. Comparison of the NRR activity for $V_3O_7 \cdot H_2O$ monolith with several recently reported electrocatalysts.

Catalyst	Electrolyte	Potential (*vs* RHE)	NH_3 yield	FE	Reference
$V_3O_7 \cdot H_2O$ monolith	**0.1M Na_2SO_4**	**-0.55V**	**36.42 μg h^{-1} $mg^{-1}_{cat.}$**	**14.20%**	**This work**
$V_3O_7 \cdot H_2O$ powder	**0.1M Na_2SO_4**	**-0.55V**	**16.52 μg h^{-1} $mg^{-1}_{cat.}$**	**8.11%**	**This work**
MXene/SSM	0.5 M Li_2SO_4	-0.10V	4.72 μg h^{-1} cm^{-2}	4.62%	1
Au Nanorod	0.1 M KOH	-0.2V	6.042 μg h^{-1} $mg^{-1}_{cat.}$	3.879%	2
Pd/C	0.1 M PBS	0.1V	4.5 μg h^{-1} $mg^{-1}_{cat.}$	8.2%	3
VN NPs	Nafion	-0.1V	3.31 × 10^{-10} mol cm^{-2} s^{-1}	5.95%	4
Mo_2C/C	0.5 M Li_2SO_4	-0.3V	11.3 μg h^{-1} mg^{-1}	7.8%	5
VNiON nanosheets/CC	0.05 M Na_2SO_4	-0.40/-0.2 V	6.78μg h^{-1} $cm^{-2}_{cat.}$	5.57	6
Dopant-free defect graphene	0.01 M H_2SO_4	-0.4V	4.31μg $h^{-1}mg^{-1}_{cat.}$	8.51%	7

B_4C/GCE	0.1 M HCl	-0.75V	26.57 μg h^{-1} $mg^{-1}_{cat.}$	15.95%	8
N-doped porous carbon	0.05 M H_2SO_4	−0.9 V	23.80 μg h^{-1} $mg^{-1}_{cat.}$	1.42%	9
Bi NS	0.1 M Na_2SO_4	-0.8V	13.23 μg h^{-1} $mg^{-1}_{cat.}$	10.49%	10
BiNCs/CB/GC	K_2SO_4 (PH=3.5)	-0.6V	200 mmol g^{-1} h^{-1}	66%	11
CoS_2/NS-G hybrids	0.05 M H_2SO_4	-0.2/-0.05V	25.0 μg h^{-1} $mg^{-1}_{cat.}$	25.9%	12
Fe_2O_3-CNT	$KHCO_3$	-2.0V	0.22 μg h^{-1} cm^{-2}	0.15%	13
Cl-GDY	0.1 M HCl	-0.45V/-0.4V	10.7μg h^{-1} cm^{-2}	8.7	14
MoS_2	0.1 M Na_2SO_4	-0.4V	2.93 μg h^{-1} cm^{-2}	8.34%	15

Supporting Reference

1. Y. Luo, G.F. Chen, L. Ding, X. Chen, L.X. Ding and H.Wang, *Joule*, 2019, **3**, 279-289.
2. D. Bao, Q. Zhang, F.L. Meng, H.X. Zhong, M.M. Shi, Y. Zhang, J.M. Yan, Q. Jiang and X.B. Zhang, *Adv. Mater.*, 2017, **29**, 1604799.
3. J. Wang, L. Yu, L. Hu, G. Chen, H. Xin and X. Feng, *Nat. Commun.*, 2018, **9**, 1795.
4. Y. Song, D. Johnson, R. Peng, D.K. Hensley, P.V. Bonnesen, L.B. Liang, J.S. Huang, F.C. Yang, F. Zhang, R. Qiao, A.P. Baddorf, T.J. Tschaplinski, N.L. Engle, M.C. Hatzell, Z.L. Wu, D.A. Cullen, H.M. Meyer, B.G. Sumpter and A.J. Rondinone, *Sci. Adv.*, 2018, **4**, e1700336.
5. H. Cheng, L.X. Ding, G.F. Chen, L. Zhang, J. Xue and H. Wang, *Adv. Mater.*, 2018, **30**, e1803694.
6. B. Chang, L. Deng, S. Wang, D. Shi, Z. Ai, H. Jiang, Y. Shao, L. Zhang, J. Shen, Y.Z.Wu and X. Hao, *J. Mater. Chem. A*, 2019, **8**, 91.
7. Y. Du, C. Jiang, W. Xia, L. Song, P. Li, B. Gao, C. Wu, L. Sheng, J. Ye, T. Wang and J. He, *J. Mater. Chem. A*, 2020, **8**, 55.
8. W. Qiu, X.Y. Xie, J. Qiu, W.H. Fang, R. Liang, X. Ren, X. Ji, G. Cui, A.M. Asiri, G. Cui, B. Tang and X. Sun, *Nat. Commun.*, 2018, **9**, 3485.
9. Y. Liu, Y. Su, X. Quan, X. Fan, S. Chen, H. Yu, H. Zhao, Y. Zhang and J. Zhao, *ACS Catal.*, 2018, **8**, 1186-1191.
10. L. Li, C. Tang, B. Xia, H. Jin, Y. Zheng and S.Z. Qiao, *ACS Catal.*, 2019, **9**, 2902-2908.

11. Y.C. Hao, Y. Guo, L.W. Chen, M. Shu, X.Y. Wang, T.A. Bu, W.Y. Gao, N. Zhang, X. Su, X. Feng, J.W. Zhou, B. Wang, C.W. Hu, A.X. Yin, R. Si, Y.W. Zhang and C.H. Yan, *Nat. Catal.*, 2019, **2**, 448-456.
12. P. Chen, N. Zhang, S. Wang, T. Zhou, Y. Tong, C. Ao, W. Yan, L. Zhang, W. Chu, C. Wu and Y. Xie, *PANS.*, 2019, **116**, 6635-6640.
13. S.Chen,S. Perathoner,C. Ampelli,C. Mebrahtu,D. Su andG. Centi, *Angew. Chem.*, *Int. Ed.*,2017, **56**, 2699-2703.
14. H. Zou, W. Rong, B. Long, Y. Ji and L. Duan, *ACS Catal.*, 2019, **9**, 10649-10655.
15. X. Li, T. Li, Y. Ma, Q.Wei, W. Qiu, H. Guo, X. Shi, P. Zhang, A.M. Asiri, L. Chen, B. Tang and X. Sun, *Adv. Energy Mater.*, 2018, **8**, 1801357.